Journal of Energy Chemistry 47 (2020) 299–306

Contents lists available at ScienceDirect

Journal of Energy Chemistry

journal homepage: www.elsevier.com/locate/jechem

http://www.journals.elsevier.com/journal-of-energy-chemistry/

Oxygen defect-rich double-layer hierarchical porous Co_3O_4 arrays as high-efficient oxygen evolution catalyst for overall water splitting

Puxuan Yan[a,b], Meilin Huang[a], Benzhi Wang[a], Zixia Wan[a], Mancai Qian[a], Hu Yan[a], Tayirjan Taylor Isimjan[c,*], Jianniao Tian[a], Xiulin Yang[a,*]

[a] Guangxi Key Laboratory of Low Carbon Energy Materials, School of Chemistry and Pharmaceutical Sciences, Guangxi Normal University, Guilin 541004, Guangxi, China
[b] School of Material Science and Engineering, Guilin University of Electronic Technology, Guilin 541004, Guangxi, China
[c] Saudi Arabia Basic Industries Corporation (SABIC) at King Abdullah University of Science and Technology (KAUST), Thuwal 23955-6900, Saudi Arabia

ARTICLE INFO

Article history:
Received 17 January 2020
Revised 8 February 2020
Accepted 10 February 2020
Available online 24 February 2020

Keywords:
Metal-organic frameworks
Array-like structure
Oxygen defects
Oxygen evolution
Water splitting

ABSTRACT

Construction of oxygen evolution electrocatalysts with abundant oxygen defects and large specific surface areas can significantly improve the conversion efficiency of overall water splitting. Herein, we adopt a controlled method to prepare oxygen defect-rich double-layer hierarchical porous Co_3O_4 arrays on nickel foam (DL-Co_3O_4/NF) for water splitting. The unique array-like structure, crystallinity, porosity, and chemical states have been carefully investigated through SEM, TEM, XRD, BET, and XPS techniques. The designated DL-Co_3O_4/NF has oxygen defects of up to 67.7% and a large BET surface area (57.4 $m^2\ g^{-1}$). Electrochemical studies show that the catalyst only requires an overpotential of 256 mV to reach 20 mA cm^{-2}, as well as a small Tafel slope of 60.8 mV dec^{-1}, which is far better than all control catalysts. Besides, the catalyst also demonstrates excellent overall water splitting performance in a two-electrode system and good long-term stability, far superior to most previously reported catalysts. Electrocatalytic mechanisms indicate that abundant oxygen vacancies provide more active sites and good conductivity. At the same time, the unique porous arrays facilitate electrolyte transport and gas emissions, thereby synergistically improving OER catalytic performance.

1. Introduction

Water splitting with zero carbon emission is regarded as an environmentally friendly choice to generate oxygen and hydrogen, of which hydrogen can alleviate the energy crisis [1]. However, the oxygen evolution reaction (OER) has a sluggish reaction kinetics during water splitting due to the elusive four-electron redox step, which requires a high overpotential to achieve a high current density [2,3]. Although noble metal-based materials (RuO_2 and IrO_2) are considered to be the most advanced benchmark electrocatalysts, their poor stability, scarcity and high cost have greatly hindered their widespread application as commercial electrocatalysts [4–6]. Therefore, there is an urgent need to research earth-abundant, inexpensive, and stable catalysts to achieve effective OER.

3d-transition metal oxides, especially Co_3O_4, have been studied intensively for developing highly efficient and low-cost alkaline OER electrocatalysts [7–9]. However, their inherent of the low conductivity has greatly limited their rapid development [10]. The OER performance of Co-based OER can be improved by regulating the intrinsic activity of the catalyst and electrode design with a high specific surface area. The introduction of oxygen defects can significantly increase the intrinsic OER activity of Co-based oxides [11]. Therefore, oxygen vacancies are one of the most studied aspects of the oxygen defect engineering in metal oxides since the surface electronic properties and gap states can be tailored by altering the concentration of oxygen vacancies [12]. Thereby much higher electrical conductivity and catalytic activity can be acquired as compared to the Co-based oxides [11]. The methods for generating oxygen vacancies include $NaBH_4$ treatment [13], Ar plasma treatment [14], and Ar/air-assisted thermal annealing [15], among which the annealing technology has good potential applications due to its simple operation, uniform vacancy distribution, and easy-to-scale production.

Generally, a working electrode is prepared by pipetting uniformly dispersed ink solution, including catalyst particles and Nafion solution on current collectors such as carbon fiber paper or glassy carbon electrode [16,17]. The electrochemically ac-

* Corresponding authors.
E-mail addresses: isimjant@sabic.com (T.T. Isimjan), xlyang@gxnu.edu.cn (X. Yang).

https://doi.org/10.1016/j.jechem.2020.02.006

tive site densities are directly proportional to the specific surface area. However, the dipping method can neither expose more active sites nor enhance electrolyte and oxygen diffusion compared with the *in-situ* formation of array-like catalysts on the electrode [18]. Therefore, fabrication of array-like structured cobalt-based oxides with high oxygen-defects holds excellent potential for highly efficient OER catalyst in an alkaline environment.

Herein, we constructed a unique core-shell structure of the oxygen defect-rich Co_3O_4 layer on the top of ZIF-67-derived hierarchical porous Co_3O_4 arrays supported by nickel foam (DL-Co_3O_4/NF). The final catalyst was prepared through in-situ ZIF-67 arrays growth, electrodeposition, plus two-stage calcination. The microscopic morphology, crystal structure, porosity, BET surface area, and chemical states of DL-Co_3O_4/NF have been carefully characterized and analyzed. Electrochemical studies show that the DL-Co_3O_4/NF catalyst exhibits the lowest overpotential (256 mV) to reach 20 mA cm^{-2} and the smallest Tafel slope (60.8 mV dec^{-1}), which is much lower than those of various control and previously reported OER catalysts. This excellent catalytic activity is the result of high electrochemical double-layer capacitance and the lowest charge transfer resistance. Besides, the DL-Co_3O_4/NF catalyst also demonstrates outstanding overall water splitting features (η_{20}=1.49 V and η_{100}=1.71 V) and long-term stability, implying a potential commercial application.

2. Experimental

2.1. Chemicals and materials

All chemicals including cobalt (II) nitrate hexahydrate ($Co(NO_3)_2{\cdot}6H_2O$), potassium hydroxide (KOH), 2-methanlimidazole, ethanol and hydrochloric acid (HCl) were analytical grade and were used directly without purification. Nickel foam with a thickness of 1.6 mm was purchased from Kunshan Jiayisheng Electronics Co. Ltd. The water was purified through a Millipore system.

2.2. Synthesis of ZIF-67/NF and Z-Co_3O_4/NF

In a typical synthesis, NF was cleaned in 0.5 M HCl, ethanol and deionized water for 15 min, respectively. The $Co(NO_3)_2{\cdot}6H_2O$ (1.6 mmol) and 2-methylimidazole (8.0 mmol) were dissolved in deionized water (20 mL) respectively, then mixed together under continuous stirring. Ten minutes later, several pieces of NF (1 cm × 1 cm) were put into the above mixture and kept for 6 h. After that, the resulted ZIF-67 modified NF (ZIF-67/NF) were took out, thoroughly washed with deionized water and dried in oven at 38 °C for 12 h. The obtained ZIF-67/NF samples were placed in a tubular furnace and carbonized at 330 °C for 6 h under N_2 atmosphere. The resulted samples were denoted as NC–Co_3O_4/NF. Then, the NC–Co_3O_4/NF sample was annealed in air at 350 °C for 2.0 h, and the obtained sample was expressed as Z-Co_3O_4/NF.

2.3. Synthesis of DL-Co_3O_4/NF and E-Co_3O_4/NF

In-situ growth of $Co(OH)_2$ on the surface of NC–Co_3O_4/NF and NF was achieved by a direct electrodeposition method. The NC–Co_3O_4/NF and NF were used as working electrodes in a typical three-electrode system and electrodeposited at −10 mA cm^{-2} for 1.0 h in 0.085 M $Co(NO_3)_2$ solution. After being washed with deionized water and dried in oven at 38 °C, the resulted samples were designated as $Co(OH)_2$@NC–Co_3O_4/NF and $Co(OH)_2$/NF, respectively. Furthermore, the obtained $Co(OH)_2$@NC–Co_3O_4/NF and $Co(OH)_2$/NF were annealed at 350 °C for 2.0 h in air atmosphere. The resulted samples were nominated as DL-Co_3O_4/NF and E-Co_3O_4/NF respectively, and the actual loading of DL-Co_3O_4 powder on NF is about 10.0 mg cm^{-2} by microbalance.

The control catalyst of RuO_2 was obtained by direct calcination of commercial $RuCl_3{\cdot}3H_2O$ at 400 °C for 3 h in air and grinded into powders. The RuO_2 powders (2.0 mg) and Nafion (5 wt%, 10 μL) were ultrasonically dispersed in ethanol (200 μL) for 30 min. The resulted inks were pipetted onto the surface of NF (1 cm × 1 cm). In addition, commercial Pt/C modified NF was prepared by the same method as above.

2.4. Characterizations

Morphology and microstructure of the synthesized materials were investigated by field emission scanning electron microscopy (SEM, FEI Quanta 600) and high-resolution transmission electron microscopy (HR-TEM, JEM-2100F). X-ray diffraction (XRD) analysis data from the samples was collected by using a Rigaku D/MAX 2500 v/pc (Japan) diffractometer with Cu *Kα* radiation. The chemical valences of the catalyst were analyzed by X-ray photoelectron spectroscopy (XPS) (JPS-9010TR, Japan) with an Mg *Kα* radiation. Nitrogen adsorption–desorption measurements were conducted on a Quantachrome AUTOSORB-IQ instrument. The specific surface area and pore size distribution were calculated according to the Brunauer–Emmett–Teller (BET) and t-Plot methods, respectively. Raman spectra were recorded using Renishaw inVia spectrometer. The electrical resistivity of various catalysts was recorded by four-point probe meter (RTS-9).

2.5. Electrochemical measurements

The electrocatalytic activity for OER was measured by the standard three-electrode system of electrochemical workstation (Biologic VMP3) with 1.0 M KOH (pH=13.5) as the electrolyte. The samples were used as the working electrode. The reference electrode and the counter electrode were saturated calomel electrode and carbon plate, respectively. Before tests, the catalysts were cycled several times via cyclic voltammetry (CV) between 0 V and 0.8 V. Linear sweep voltammetry (LSV) was carried out at a scan rate of 2 mV s^{-1}.

The potential of E_{RHE} was calibrated by the equation of $E_{RHE} = E_{SCE}+0.241+0.059\ pH = E_{SCE}+1.037$, which is consistent with the RHE voltage calibration result of 1.037 V (Fig. S1). All the LSV polarization curves were corrected by the equation of $E_{cor} = E_{RHE}-iR_s$, where E_{cor} is the corrected potential (V), i is the test current (A), and R_s is the solution resistance obtained from electrochemical impedance spectroscopy (EIS, Ω). The EIS measurements were performed at 1.54 V (vs. RHE) with frequencies from 200 kHz to 0.1 Hz. The stability of the samples was investigated by chronopotentiometry at varying current densities of 10, 20 and 50 mA cm^{-2}, respectively. The overall water splitting test was performed by two-electrode system in the potential range of 0~2.0 V with a scan rate of 2 mV s^{-1}, and the presented curve was after iR_s-compensation.

The double layer capacitance (C_{dl}) of all catalysts were studied in non-faradaic potential windows in 1.0 M KOH. The scan rates were changed from 1 to 10 mV s^{-1}, and the C_{dl} was calculated by the equation of $C_{dl} = (j_a-j_c)/(2 \times \nu)$, where j_a and j_c is the respective current density of anode and cathode, and ν is the scan rate.

3. Results and discussion

3.1. Synthetic strategy analysis

Scheme 1 presents the schematic illustration of preparing Co_3O_4 layers on ZIF-67 derived Co_3O_4 arrays/NF. The ZIF-67 was used as the carbon and metal source which forms a uniform metal distributed conductive carbon layer after calcination [5,19]. In this work, NF was selected as the substrate for the in-situ growth of

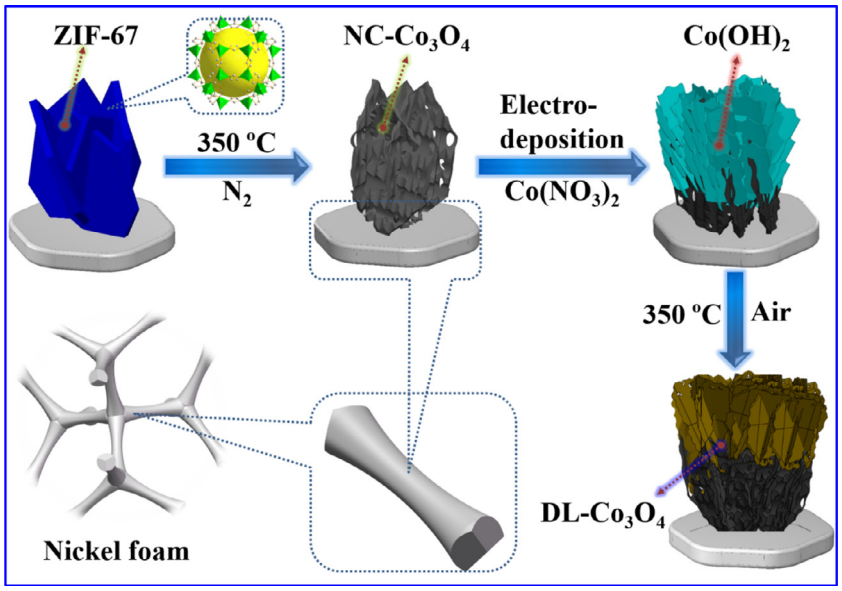

Scheme 1. Schematic illustration of the formation process of DL-Co_3O_4/NF.

ZIF-67, and the loading of ZIF-67 can be controlled by altering the growth time and the precursor's concentration. As shown in Fig. S2, the NF surface was covered evenly by blue-colored ZIF-67. The ZIF-67 loading is ca. 7.4 mg cm^{-2}. Thermogravimetric analysis indicates that ZIF-67 has two strong exothermic peaks in N_2 atmosphere, where the 290 °C peak indicates intermolecular dehydration and the 498 °C peak is the starting point of carbonization process (Fig. S3). The optical photograph further confirms that the annealed products of ZIF-67/NF present different colors at different temperatures, for example, blue (200 °C), yellow (250 °C), reddish-brown (300 °C) and black (≥350 °C) in N_2 atmosphere (Fig. S4), indicating the formation of various intermediate states during the pyrolysis. Among them, the sample NC–Co_3O_4/NF prepared at 350 °C was selected as the intermediate material. After that, the second layer of $Co(OH)_2$ was electrodeposited onto the surface of NC–Co_3O_4/NF to build a double-layer $Co(OH)_2$@NC–Co_3O_4/NF composite which was further annealed at 350 °C in air subsequently to obtain the defect-rich DL-Co_3O_4/NF. The results reveal that the DL-Co_3O_4/NF composite (XRD) prepared by two-step calcination method has the largest specific surface area and the highest conductivity (Table S1) [20]. Moreover, the core-shell structure helps to eliminate structural defects in the inner layer and enhance the thermostability thereof improves the performance of the materials, which is widely applied in nanoparticle synthesis [21].

3.2. Microstructure, crystallinity and porosity analysis

Scanning electron microscopy (SEM) images were used to characterize the topographical changes of a series of materials. As shown in Fig. 1(a), the ZIF-67 grows vertically on the surface of NF with interpenetrating sheet-like structures. After calcination in N_2, the vertically distributed sheet-like architectures remained while having an apparent porosity (Fig. 1b). A large number of densely sheet-like structures are exposed on the outer surface (Fig. 1c) after the subsequent electrodeposition of $Co(OH)_2$ layers. Interestingly, we can observe that the resulted DL-Co_3O_4/NF composite contains numerous interconnected thin-film structures with large pores after calcination in the air (Fig. 1d). The cross-sectional SEM image shows that the thickness of the Co_3O_4 layers obtained from ZIF-67 and $Co(OH)_2$ species are approximately 3.6 and 1.5 um, respectively (Fig. S5). The unique morphology is beneficial for exposing active sites, improving electrolyte, and mass transports, thereof expected to provide robust electrocatalytic performance.

To further examine the microscopic features of DL-Co_3O_4/NF, detailed transmission electron microscopy (TEM) studies were undertaken. The DL-Co_3O_4 arrays were peeled off from the substrate of NF and distributed in ethanol solution. Then it was pipetted onto a copper grid pre-coated with a holey carbon film. The copper grid was transferred into TEM with an operating voltage of 200 kV. As shown in Fig. 2(a), a plurality of particulate materials mainly composes the sheet-like structures. The inset of high-resolution TEM exhibits two types of well-defined lattice spacings of 0.243 and 0.467 nm, which can be assigned to the (111) and (220) crystal planes of Co_3O_4 (JCPDS: 42–1467). Moreover, the corresponding selected area electron diffraction (SAED) displays concentric diffraction rings made up of discrete spots (Fig. 2b), which are indexed to the (111), (220) and (311) planes of cubic Co_3O_4 as well. Moreover, Raman spectrum was also used to detect DL-Co_3O_4 and control samples, and some distinctive scattering peaks such as A_{1g} (690.1 cm^{-1}), F_{2g} (620.0 cm^{-1}), F_{2g} (523.5 cm^{-1}), E_g (480.9 cm^{-1}), and F_{2g} (194.6 cm^{-1}) were observed (Fig. S6), further indicating the presence of Co_3O_4 species in the composites [22]. The crystal structures of as-prepared materials are investigated by X-ray diffraction (XRD) patterns. As shown in Fig. 2(c), the diffraction peaks of ZIF-67 are consistent with the reported ZIF-67 in the literature [23,24]. After the carbonization procedure, ZIF-67 is wholly converted to Co_3O_4 (JCPDS: 42–1467). It is worth noting that the electrodeposited Co species mainly exists in the form of $Co(OH)_2$ (JCPDS: 30–0443) before annealing, which was converted into to Co_3O_4 species upon annealing. The isotherms of the samples exhibit the typical H3-type hysteresis loop in Fig. 2(d). The BET specific surface area of DL-Co_3O_4 arrays is calculated to be 57.4 m^2 g^{-1}, which is much higher than that of Z-Co_3O_4 (27.9 m^2 g^{-1}). The adsorption average pore diameters of DL-Co_3O_4 and Z-Co_3O_4 are about 12.6 and 16.5 nm, respectively, which are mainly caused by flaky cracks of the composites. The larger BET surface area of DL-Co_3O_4/NF composite provides more active sites as well as better mass transfer thereof, helping to improve the OER performance.

3.3. XPS analysis

The composition and chemical states of DL-Co_3O_4/NF were further examined by X-ray photoelectron spectroscopy (XPS). As

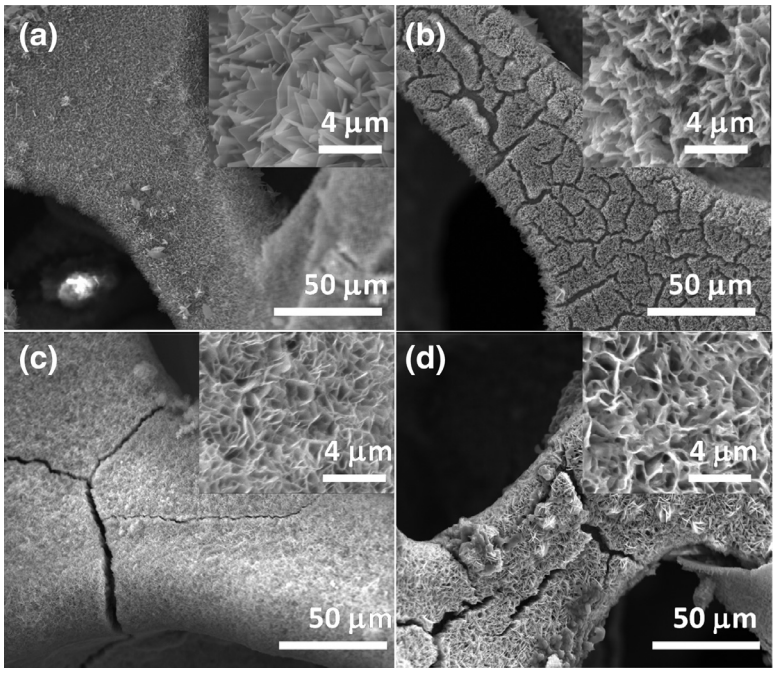

Fig. 1. SEM images of (a) ZIF-67/NF, (b) NC–Co_3O_4/NF, (c) $Co(OH)_2$@NC–Co_3O_4/NF and (d) DL-Co_3O_4/NF with different magnifications.

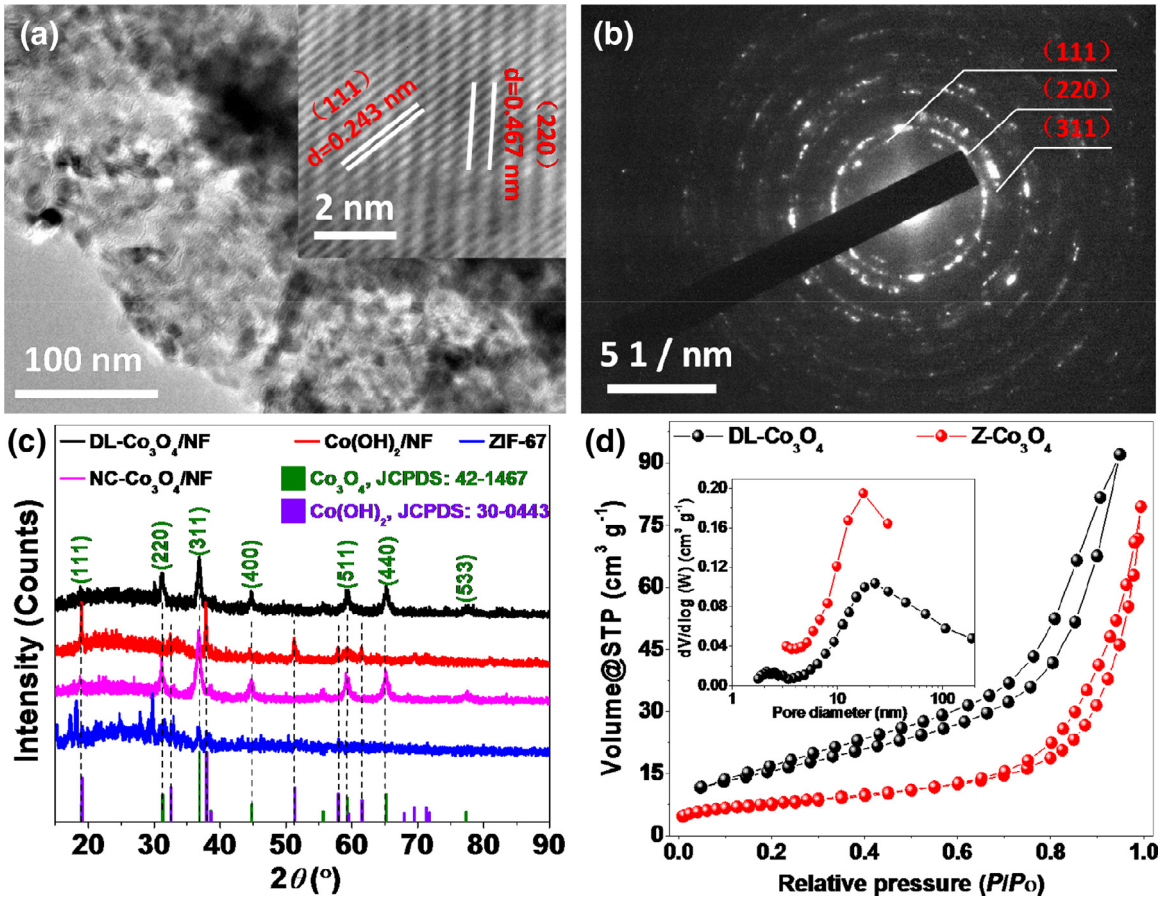

Fig. 2. (a) TEM (Inset of HR-TEM) and (b) SAED images of DL-Co_3O_4/NF. (c) XRD patterns of different composites. (d) Nitrogen adsorption–desorption isotherms of Z-Co_3O_4 and DL-Co_3O_4 arrays.

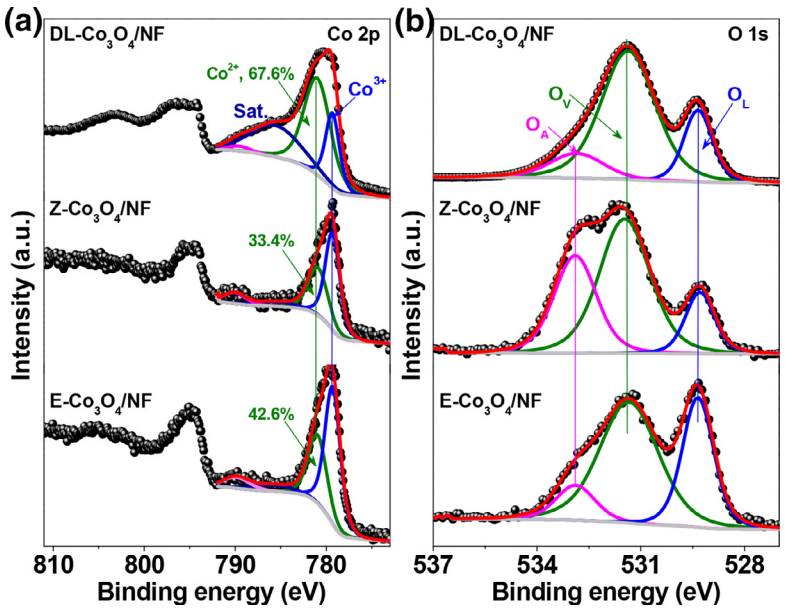

Fig. 3. High-resolution X-ray photoelectron spectroscopy (XPS) of (a) Co 2*p* and (b) O 1*s* for DL-Co_3O_4/NF, Z-Co_3O_4/NF and E-Co_3O_4/NF, respectively.

shown in Fig. S7, the high-resolution C 1*s* spectrum of DL-Co_3O_4/NF is convoluted into C = C (284.0 eV), C–C (284.8 eV) and C–O (286.0 eV) used as calibration standard [25,26]. Fig. 3(a) shows the high-resolution Co 2*p* core-level spectrum, where the characteristic peaks at 779.3 eV correspond to Co^{3+}, and the peaks at 781.0 eV can be attributed to Co^{2+}, indicating the coexistence of Co^{2+} and Co^{3+} species [27]. It can be observed that the area percentage of Co^{2+} species on the surface of DL-Co_3O_4/NF (67.6%) is significantly higher than those of Z-Co_3O_4/NF (33.4%) and E-Co_3O_4/NF (42.6%) catalysts. The higher Co^{2+} content on the surface implies more oxygen vacancies [28], in which the tetrahedral Co^{2+} sites in the Co_3O_4 skeleton tend to form cobalt oxyhydroxide based catalytic centers for water oxidation [29]. In addition, high-resolution O 1s XPS spectra are used to detect the changes in oxygen species on different catalyst surface (Fig. 3b), where the binding energies at 529.3, 531.3, and 532.8 eV are ascribed to the lattice oxygen (denoted as O_L), oxygen vacancies (denoted as O_V) [30], and absorbed oxygen species (denoted as O_A) in the cobalt oxide [31,32], respectively. The area percentage of O_v is obtained by integrating the fitted component area from the XPS spectrum [33]. The O_v percentage of DL-Co_3O_4/NF is ca. 67.7%, which is substantially higher than those of Z-Co_3O_4/NF (53.6%) and E-Co_3O_4/NF (56.7%). The high Co^{2+} content and abundant O_v species can be understood as when the oxygen leaves from the surface as an oxygen molecule, it leaves two electrons behind that reduce Co^{3+} to Co^{2+} [34]. Therefore, the higher Co^{2+} content indicates more O_v. Moreover, it was reported that a more elevated the O_v has better catalytic performance [11], which is also confirmed in this study.

3.4. Electrochemical analysis

LSV polarization curves were used to evaluate the OER performances of various catalysts in a typical three-electrode electrochemical cell in 1.0 M KOH solution. As shown in Fig. 4(a), the DL-Co_3O_4/NF catalyst requires a lower overpotential of 256 mV to reach 20 mA cm^{-2}, which is significantly lower than those of Z-Co_3O_4/NF (330.7 mV), E-Co_3O_4/NF (283.0 mV), RuO_2/NF (278.4 mV), and NF (442.2 mV). It should be noted that the overpotential at 20 mA cm^{-2} was used instead of 10 mA cm^{-2} for comparison due to the strong redox peaks interfere with the measurements as shown in Fig. 4(a). As a result, the measured overpotential of NF is larger than these reported at 10 mA cm^{-2}. However, the overpotential of NF (442.2 mV) in this study is in the range of these published elsewhere [35,36]. Besides, the superior OER electrocatalytic activity is also accompanied by a small Tafel slope. As shown in Fig. 4(b), the Tafel slope of the DL-Co_3O_4/NF catalyst is 60.8 mV dec^{-1}, which is much lower than those of other control catalysts indicating the fastest OER kinetic [37]. Furthermore, Fig. 4(c) further demonstrates that the designed catalyst, both in terms of overpotential and Tafel slope, is far superior to most recently reported OER catalysts under similar conditions (Table S2).

The number of catalytically active sites on the catalyst surface can be evaluated by the electrochemically active surface area (ECSA) measurement. At the same time, the ECSA is directly proportional to the electrochemical double-layer capacitance (C_{dl}) [38]. The C_{dl} value is obtained by CV curves of the catalyst with different scan rates in a non-faradaic potential region (Fig. S8). Fig. 4(d) presents that the DL-Co_3O_4/NF catalyst has a C_{dl} value of 275.1 mF cm^{-2}, which is approximately 9.3-, 3.7- and 7.4-fold more significant than those of Z-Co_3O_4/NF, E-Co_3O_4/NF, and RuO_2/NF, respectively. It should be emphasized that the differences in the capacitances are consistent with the changes in the electrochemical activity of these catalysts meaning higher C_{dl} better the electrochemical activity. This result implies that the hierarchical porous structure, as well as abundant active sites, are the main reasons for promoting OER activity.

The Nyquist plots were obtained from electrochemical impedance spectroscopy (EIS), revealing the charge-transfer resistances at the catalyst/electrolyte interface [39]. In general, the intersection of the semicircles at the X-axis presents the solution resistance (R_s). The semicircle diameter can be attributed to the charge transfer resistance (R_{ct}) of the catalyst [18]. As shown in Fig. S9, the DL-Co_3O_4/NF exhibited the smallest semicircular diameters compared to all control catalysts, indicating a faster charge transferability due to the larger interfacial contact areas with the electrolyte and shorter ion diffusion paths resulting from their unique nanostructures [40].

The two-electrode water splitting test is a crucial indicator of whether a catalyst can be commercialized. Fig. 5(a) is a schematic depiction of electrocatalytic water splitting in a two-electrode system. As shown in Fig. 5(b), we constructed a device using a commercial Pt/C modified NF as the cathode and the designed DL-

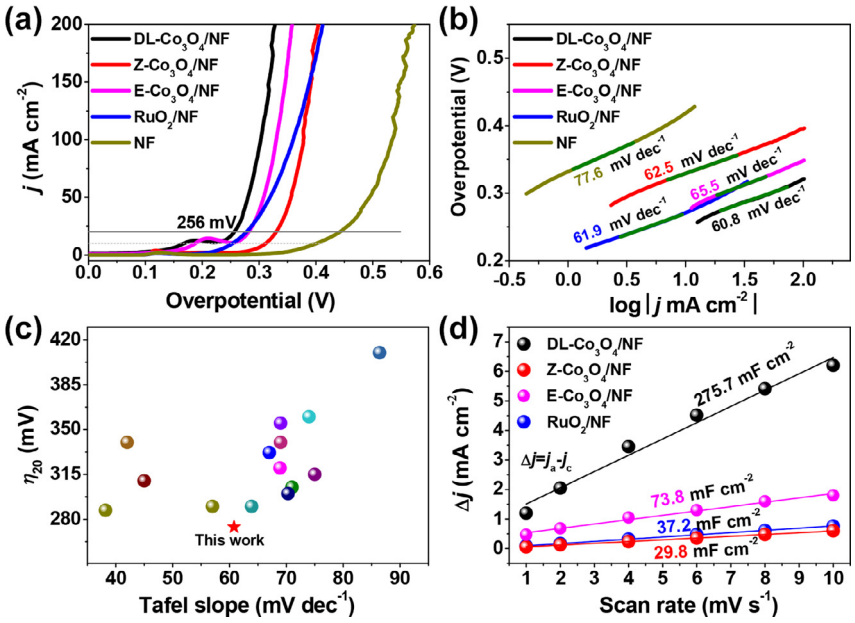

Fig. 4. (a) OER polarization curves of DL-Co_3O_4/NF together with Z-Co_3O_4/NF, E-Co_3O_4/NF, RuO_2/NF and NF in 1.0 M KOH. (b) The corresponding Tafel slopes from (a). (c) Compared with the overpotential (η_{20} at 20 mA cm^{-2}) and Tafel slope of different OER catalysts reported in recent literature. (d) Charge current density differences (Δj) plotted against scan rates for different catalysts.

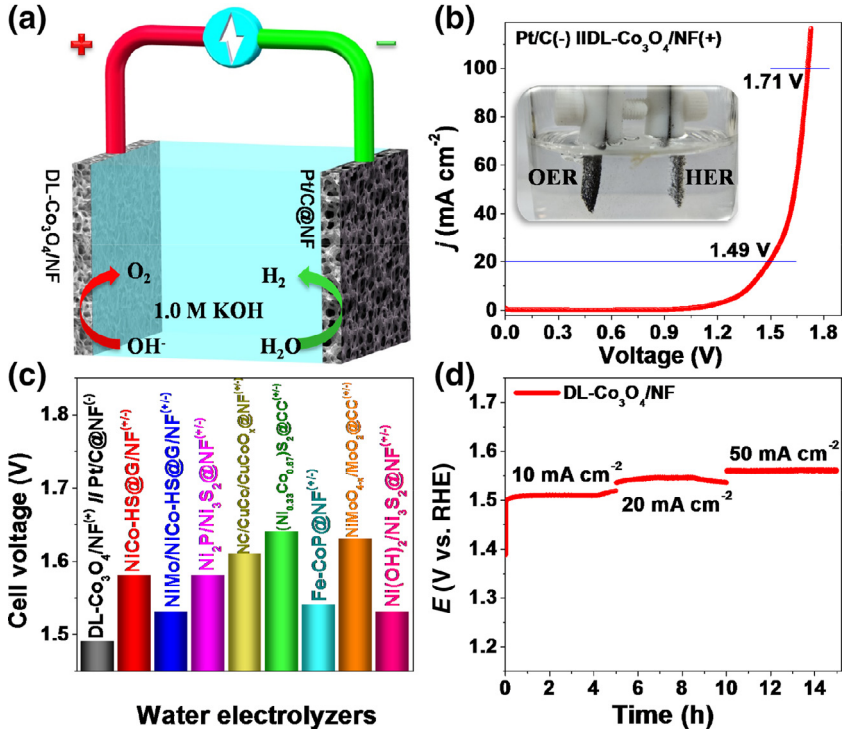

Fig. 5. (a) Schematic description of overall water splitting in two-electrode system. (b) Overall water splitting of the designed DL-Co_3O_4/NF and commercial Pt/C as anode and cathode electrocatalysts in 1.0 M KOH solution. (c) Compare the cell voltages of the currently available electrolytic cells at 20 mA cm^{-2} in 1.0 M KOH. (d) Chronopotentiometry curves of DL-Co_3O_4/NF at the different current densities.

Co_3O_4/NF catalyst as an anode. We investigated the catalytic performance for overall water splitting in a two-electrode system. It can be found that the DL-Co_3O_4/NF(OER)//Pt (HER) based two-electrode system only needs about 1.49, and 1.71 V to reach 20 and 100 mA cm^{-2} in 1.0 M KOH solution. Those results are significantly lower than most recently reported two-electrode catalytic systems (Fig. 5c and Table S3) [4,6,41–45]. The catalyst stability was investigated using the chronopotentiometry. The potentials changes at the constant current densities (10, 20, and 50 mA cm^{-2}) in a three-electrode system were monitored with the time (Fig. 5d). The results show that the DL-Co_3O_4/NF catalyst exhibits excellent stability after continuous operation for 15 h. However, the surface porosity was decreased, and the material became more compact, as shown in Fig. S10.The unusual two-electrode catalytic activity and long-term stability are the outcomes of the highly conductive array-like morphology along with the abundant active sites.

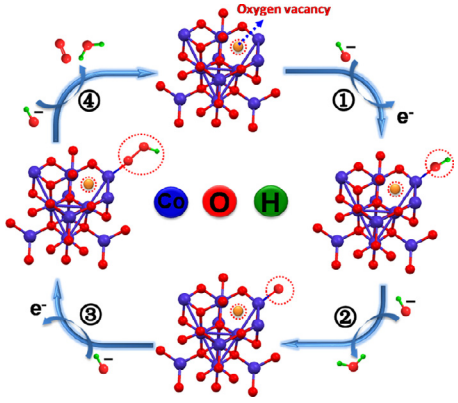

Scheme 2. The proposed catalytic mechanism of DL-Co_3O_4/NF catalyst for OER in alkaline media.

3.5. Catalytic mechanism analysis

As we discussed above, the excellent OER performance is the combined effects of the abundant active sites as well as the sizeable electrical conductivity of the designed catalysts. In this work, the ample oxygen vacancies in DL-Co_3O_4/NF are formed due to the detachment of partial oxygen in the lattice of Co_3O_4 under 350 °C annealing conditions. The neighboring Co atoms can be significantly regulated to create new active sites and increase the conductivity, thereby reducing the Gibbs free energy in the OER conversion steps and greatly enhancing the OER catalytic activity [46]. A schematic diagram of the OER catalytic mechanism is described in Scheme 2. The three fundamental steps of the OER process on DL-Co_3O_4/NF include adsorption, dissociation, and desorption [47]. The formation of *OH, *O, and *OOH intermediates are reconciled with the utilization of surface Co atom. Previous DFT calculations revealed that the oxygen vacancies created new defect states in the band gap of Co_3O_4, and the electrons adjacent to the oxygen vacancies that previously occupied the O 2*p* orbital were delocalized, thereof the surface with the oxygen vacancies was much more activated [48]. Meanwhile, the delocalized electrons near the oxygen vacancies are easily excited to the conduction band, thereby increasing the conductivity of Co_3O_4 and significantly improving the OER catalytic activity [13,49].

4. Conclusions

In summary, the oxygen defect-rich DL-Co_3O_4/NF catalyst was fabricated by a controllable four-step. The steps are *in-situ* growth of ZIF-67, calcination, electrodeposition of $Co(OH)_2$, and air oxidation. The SEM, TEM, and BET analyses confirmed the presence of porous array structures. Moreover, the XPS results indicated the highest proportion of oxygen defects on the designed catalyst surface as compared to others. In addition, the four-probe measurement and electrochemical impedance test demonstrated high conductivity and small resistance. Electrochemical measurement results show that the DL-Co_3O_4/NF catalyst has the lowest overpotential, the smallest Tafel slope, the best OER performance, and superior stability among the other OER catalysts. The excellent OER performance is the combined effects of the unique array-like structure, abundant electrocatalytic active sites, and high electrical conductivity.

Declaration of Competing Interests

The authors declare that they have no known competing financial interests or personal relationships that could have appeared to influence the work reported in this paper.

Acknowledgments

This work has been supported by the National Natural Science Foundation of China (no. 21965005), Natural Science Foundation of Guangxi Province (2018GXNSFAA294077, 2018GXNSFAA281220), Project of High-Level Talents of Guangxi (F-KA18015, 2018ZD004) and Innovation Project of Guangxi Graduate Education (XYCSZ2019056, YCBZ2019031).

Supplementary materials

Supplementary material associated with this article can be found, in the online version, at doi:10.1016/j.jechem.2020.02.006.

References

[1] F. Sun, G. Wang, Y. Ding, C. Wang, B. Yuan, Y. Lin, Adv. Energy Mater. 8 (2018) 1800584.
[2] P. Li, H.C. Zeng, Adv. Funct. Mater. 27 (2017) 1606325.
[3] M. Gong, Y. Li, H. Wang, Y. Liang, J.Z. Wu, J. Zhou, J. Wang, T. Regier, F. Wei, H. Dai, J. Am. Chem. Soc. 135 (2013) 8452–8455.
[4] T. Tang, W.-J. Jiang, S. Niu, N. Liu, L. Hao, Q. Zhang, W. Wen, Y.-Y. Chen, L.-B. Huang, F. Gao, J.-S. Hu, Adv. Funct. Mater. 28 (2017) 1704594.
[5] B.Y. Xia, Y. Yan, N. Li, H.B. Wu, X. Wen Lou, X. Wang, Nat. Energy 1 (2016) 15006.
[6] L. Zeng, K. Sun, X. Wang, Y. Liu, Y. Pan, Z. Liu, D. Cao, Y. Song, S. Liu, C. Liu, Nano Energy 51 (2018) 26–36.
[7] F. Lyu, Y. Bai, Z. Li, W. Xu, Q. Wang, J. Mao, l. Wang, X. Zhang, Y. Yin, Adv. Funct. Mater. (2017) 1702324.
[8] J. Qi, W. Zhang, R. Cao, Chem. Commun. 53 (2017) 9277–9280.
[9] A. Kumar, S. Bhattacharyya, ACS Appl. Mater. Interfaces 9 (2017) 41906–41915.
[10] H. Mistry, Y.-W. Choi, A. Bagger, F. Scholten, C. Bonifacio, I. Sinev, N.J. Divins, I. Zegkinoglou, H.S. Jeon, K. Kisslinger, E.A. Stach, J.C. Yang, J. Rossmeisl, B. Roldán Cuenya, Angew. Chem.-Int. Edit. 56 (2017) 11394–11398.
[11] R. Zhang, Y.-C. Zhang, L. Pan, G.-Q. Shen, N. Mahmood, Y.-H. Ma, Y. Shi, W. Jia, L. Wang, X. Zhang, W. Xu, J.-J. Zou, ACS Catal. 8 (2018) 3803–3811.
[12] C.M. Boudreaux, N.P. Liyanage, H. Shirley, S. Siek, D.L. Gerlach, F. Qu, J.H. Delcamp, E.T. Papish, Chem. Commun. 53 (2017) 11217–11220.
[13] Y. Liu, W. Wang, H. Huang, L. Gu, Y. Wang, X. Peng, Chem. Commun. 50 (2014) 4485–4488.
[14] Y. Lu, A. Ma, Y. Yu, R. Tan, C. Liu, P. Zhang, D. Liu, J. Gui, ACS Sustainable Chem. Eng. 7 (2019) 2906–2910.
[15] F. Cheng, T. Zhang, Y. Zhang, J. Du, X. Han, J. Chen, Angew. Chem. Int. Ed. 52 (2013) 2474–2477.
[16] G. Ou, F. Wu, K. Huang, N. Hussain, D. Zu, H. Wei, B. Ge, H. Yao, L. Liu, H. Li, Y. Shi, H. Wu, ACS Appl. Mater. Interfaces 11 (2019) 3978–3983.
[17] Y.-Z. Jin, Z. Li, J.-Q. Wang, R. Li, Z.-Q. Li, H. Liu, J. Mao, C.-K. Dong, J. Yang, S.-Z. Qiao, X.-W. Du, Adv. Energy Mater. 8 (2018) 1703469.
[18] A.A.A. Talha, H. Bo, C.H. S., J. Yongcheol, C. Sangeun, K. Jongmin, P.S. M., C. SeungNam, I.A. I., K. Hyungsang, I. Hyunsik, Small 14 (2018) 1800742.
[19] A. Sivanantham, P. Ganesan, L. Estevez, B.P. McGrail, R.K. Motkuri, S. Shanmugam, Adv. Energy Mater. 8 (2018) 1702838.
[20] J. Zhao, X. Quan, S. Chen, Y. Liu, H. Yu, ACS Appl. Mater. Interfaces 9 (2017) 28685–28694.
[21] R. Ghosh Chaudhuri, S. Paria, Chem. Rev. 112 (2012) 2373–2433.
[22] T. Yao, X. Guo, S. Qin, F. Xia, Q. Li, Y. Li, Q. Chen, J. Li, D. He, Nano-Micro Lett. 9 (2017) 38.
[23] X. Guo, T. Xing, Y. Lou, J. Chen, J. Solid State Chem. 235 (2016) 107–112.
[24] W. Sun, X. Zhai, L. Zhao, Chem. Eng. J. 289 (2016) 59–64.
[25] J. Guo, C. Wu, J. Zhang, P. Yan, J. Tian, X. Shen, T.T. Isimjan, X. Yang, J. Mater. Chem. A 7 (2019) 8865–8872.
[26] J. Guo, B. Wang, D. Yang, Z. Wan, P. Yan, J. Tian, T.T. Isimjan, X. Yang, Appl. Catal. B: Environ. 265 (2020) 118584.
[27] M. Qian, X. Cheng, T. Sun, J. Tian, T.T. Isimjan, Z. Shi, X. Yang, J. Alloys Compd. 819 (2020) 153015.
[28] J. Yu, Q. Cao, Y. Li, X. Long, S. Yang, J.K. Clark, M. Nakabayashi, N. Shibata, J.-J. Delaunay, ACS Catal. 9 (2019) 1605–1611.
[29] Y. Tong, H. Mao, Y. Xu, J. Liu, Inorg. Chem. Front. 6 (2019) 2055–2060.
[30] D. Ding, K. Shen, X. Chen, H. Chen, J. Chen, T. Fan, R. Wu, Y. Li, ACS Catal. (2018) 7879–7888.
[31] X. Yang, J. Chen, Y. Chen, P. Feng, H. Lai, J. Li, X. Luo, Nano-Micro Lett. 10 (2018) 15.
[32] Q. Gan, X. Cheng, J. Chen, D. Wang, B. Wang, J. Tian, T.T. Isimjan, X. Yang, Electrochim. Acta 301 (2019) 47–54.
[33] Y. Zhou, C.-K. Dong, L.L. Han, J. Yang, X.-W. Du, ACS Catal. 6 (2016) 6699–6703.
[34] X. Yang, H. Li, A.-Y. Lu, S. Min, Z. Idriss, M.N. Hedhili, K.-W. Huang, H. Idriss, L.-J. Li, Nano Energy 25 (2016) 42–50.
[35] A.T. Aqueel Ahmed, B. Hou, H.S. Chavan, Y. Jo, S. Cho, J. Kim, S.M. Pawar, S. Cha, A.I. Inamdar, H. Kim, H. Im, Small 14 (2018) 1800742.
[36] Z. Wu, X. Wang, J. Huang, F. Gao, J. Mater. Chem. A 6 (2018) 167–178.
[37] M. Chauhan, K.P. Reddy, C.S. Gopinath, S. Deka, ACS Catal. 7 (2017) 5871–5879.

[38] Y. Feng, C. Xu, E. Hu, B. Xia, J. Ning, C. Zheng, Y. Zhong, Z. Zhang, Y. Hu, J. Mater. Chem. A 6 (2018) 14103–14111.
[39] Y. Zhao, J. Zhang, X. Guo, H. Fan, W. Wu, H. Liu, G. Wang, J. Mater. Chem. A 5 (2017) 19672–19679.
[40] C. Luan, G. Liu, Y. Liu, L. Yu, Y. Wang, Y. Xiao, H. Qiao, X. Dai, X. Zhang, ACS Nano 12 (2018) 3875–3885.
[41] J. Hou, Y. Sun, Y. Wu, S. Cao, L. Sun, Adv. Funct. Mater. 28 (2018) 1704447.
[42] Y.-Q. Wang, L. Zhao, X.-L. Sui, D.-M. Gu, Z.-B. Wang, Ceram. Int. 45 (2019) 17128–17136.
[43] L.-M. Cao, Y.-W. Hu, S.-F. Tang, A. Iljin, J.-W. Wang, Z.-M. Zhang, T.-B. Lu, Adv. Sci. 5 (2018) 1800949.
[44] Y. Chen, S. Yoo, y. Choi, J.H. Kim, Y. Ding, K. Pei, R. Murphy, Y. Zhang, B. Zhao, W. Zhang, H. Chen, Y. Chen, W. Yuan, C. Yang, M. Liu, Energy Environ. Sci. 11 (2018) 2458–2466.
[45] Q. Xu, H. Jiang, H. Zhang, Y. Hu, C. Li, Appl. Catal. B: Environ. 242 (2019) 60–66.
[46] Z. Wang, W. Xu, X. Chen, Y. Peng, Y. Song, C. Lv, H. Liu, J. Sun, D. Yuan, X. Li, X. Guo, D. Yang, L. Zhang, Adv. Funct. Mater. 29 (2019) 1902875.
[47] M. Fang, G. Dong, R. Wei, J.C. Ho, Adv. Energy Mater. 7 (2017) 1700559.
[48] J. Bao, X. Zhang, B. Fan, J. Zhang, M. Zhou, W. Yang, X. Hu, H. Wang, B. Pan, Y. Xie, Angew. Chem.-Int. Edit. 54 (2015) 7399–7404.
[49] L. Zhuang, L. Ge, Y. Yang, M. Li, Y. Jia, X. Yao, Z. Zhu, Adv. Mater. 29 (2017) 1606793.